Geometrical-optics solution to light scattering by droxtal ice crystals

Zhibo Zhang, Ping Yang, George W. Kattawar, Si-Chee Tsay, Bryan A. Baum, Yongxiang Hu, Andrew J. Heymsfield, and Jens Reichardt

We investigate the phase matrices of droxtals at wavelengths of 0.66 and 11 μm by using an improved geometrical-optics method. An efficient method is developed to specify the incident rays and the corresponding impinging points on the particle surface necessary to initialize the ray-tracing computations. At the 0.66-μm wavelength, the optical properties of droxtals are different from those of hexagonal ice crystals. At the 11-μm wavelength, the phase functions for droxtals are essentially featureless because of strong absorption within the particles, except for ripple structures that are caused by the phase interference of the diffracted wave. © 2004 Optical Society of America

OCIS codes: 010.1290, 010.3920, 010.1310, 290.5850, 290.1310, 280.1310.

1. Introduction

Cirrus clouds play an important role in the energy budget balance of the Earth–atmosphere system (e.g., Liou,[1] Lynch *et al.*,[2] and references cited therein). Radiative transfer modeling efforts have been hampered by the nonspherical nature of observed ice crystals in the atmosphere. Over the past several decades, substantial research efforts[3–11] have focused on deriving the single-scattering properties (e.g., single-scatter albedo and phase function) of nonspherical ice crystals, which are fundamentally important to the interpretation of the remote sensing measurements of cirrus clouds and the parameterization of the bulk radiative properties of these clouds in climate models (e.g., Mishchenko *et al.*[12] and Liou *et al.*[13]). *In situ* measurements of cirrus indicate that both the habit and the size distribution of ice crystals tend to vary with height within the clouds (e.g., Heymsfield and Iaquinta[14] and Lawson *et al.*[15]).

Small ice crystals with aspect ratios of approximately unity (i.e., the ratio of particle length to its width), often referred to as quasi-spherical particles, are predominant in the uppermost portions of midlatitude and tropical cirrus clouds.[16] If the small particles are assumed to be spherical, one can apply the Lorenz–Mie theory to calculate the single-scattering properties of these small particles. However, *in situ* observations have confirmed that these ice crystals are faceted and thus nonspherical.[17,18]

Previous research indicates that the bidirectional reflectance is highly sensitive to the geometry of the small ice crystals in the uppermost region of cirrus clouds.[19] Most recently, McFarquhar *et al.*[20] showed the importance of small ice crystals in parameterizing the bulk radiative properties of cirrus clouds. The small ice crystals were treated as Chebyshev particles, and the *T*-matrix method[21] was used to derive their scattering properties. Reichardt *et al.*[22] showed that lidar-based retrievals of polar stratospheric clouds are quite sensitive to the shape of small ice crystals. Liu and Mishchenko[23] treated small ice crystals as spheroids in their study of polar stratospheric clouds on the basis of lidar returns. Yang *et al.*[24] speculated that small ice particles observed in Alaskan ice fogs[25,26] may be similar to the shapes of the nonspherical small ice crystals in cirrus clouds. As we discuss in Section 2, droxtallike crystals have also been observed in wave clouds and may be associated with the freezing of supercooled water droplets and subsequent growth by water-vapor dep-

Z. Zhang and P. Yang (pyang@ariel.met.tamu.edu) are with the Department of Atmospheric Sciences, Texas A&M University, College Station, Texas 77843. G. W. Kattawar is with the Department of Physics, Texas A&M University, College Station, Texas 77843. S.-C. Tsay is with NASA Goddard Space Flight Center, Greenbelt, Maryland 20771. B. A. Baum and Y. Hu are with NASA Langley Research Center, Hampton, Virginia 23681. A. J. Heymsfield is with the National Center for Atmospheric Research, Boulder, Colorado 80307. J. Reichardt is with Deutscher Wetterdienst, Meteorologisches Observatorium, Lindenberg, Tauche 15848, Germany.

Received 19 July 2003; revised manuscript received 6 January 2004; accepted 4 February 2004.

0003-6935/04/122490-10$15.00/0

osition. In this situation, the rapid transition from supercooled water droplets to ice crystals through the homogeneous ice nucleation process, coupled with small amounts of available water vapor, may inhibit the development of more pristine particles such as hexagonal columns and plates.[26]

The single-scattering properties of ice droxtals have been investigated for the case of small size parameters by the finite-difference time-domain (FDTD) method.[24] Substantial differences were noted between the single-scattering properties for ice spheres and those for droxtals, especially at visible wavelengths. Because of computational limitations, the largest size parameter for a practical application of the FDTD method is approximately 20, although it has been applied to size parameters up to 40 when no attempt is made to average the scattering properties over particle orientation.[27] For a droxtal with a size parameter of 20 defined with respect to the corresponding circumscribing sphere, the effective diameter is only 4.2 μm for a wavelength of 0.66 μm. Observations show that these small particles with aspect ratios of the order of unity are present at sizes greater than 30 μm.

To obtain scattering properties for crystal sizes larger than those allowed by the FDTD method requires the development and application of various approximate approaches such as the geometrical-optics (GO) method. Many exact and approximate scattering methods have been recently reviewed by Mishchenko *et al*.[28] and Kahnert.[29] The GO method is applicable when the size of an equivalent volume sphere for the particle is much larger than the wavelength of the incident beam. The applicability of the GO method has been investigated by its comparison with the *T*-matrix method[30,31] and the FDTD method.[32,33] The theoretical framework of the GO method to compute the scattering properties of ice crystals is well established and is not repeated here.

In this study we employ the improved geometrical-optics (IGO) method developed by Yang and Liou[34] to compute the single-scattering properties of droxtals. For simplicity in software development and computational efficiency, we use a simplified version of the IGO method (see Section 3 in Ref. 34). In the simplified IGO method, the phase interference of the electric field associated with the scattered rays is accounted for approximately when we consider the ray spreading. The technical details for the simplification can be found in Yang and Liou.[34] Because of the approximate nature of the IGO method, the present scattering computations are limited to size parameters in the GO regime.

2. Droxtal Geometry and Coordinate Frame

Figure 1 shows images of droxtals collected in an orographic wave cloud that was penetrated by a balloonborne ice crystal replicator in Colorado. The wave cloud temperature ranged from −40 °C to −56 °C, and throughout the layer particles were present in high concentrations (~1 cm^{-3}) and were fairly uniform in size. The lines shown in the right panel of Fig. 1 indicate the size scale; the distance between the two adjacent lines is 10 μm. The droxtals shown here are of the order of 30 μm in diameter. Close scrutiny of these and other particle images indicates that these particles are not spherical. Ohtake[26] provided more detailed images and noted the three-dimensional structure of these small particles. Situations that are particularly amenable to droxtal production occur when the homogeneous ice nucleation process is active, at temperatures below −35 °C, and include orographic wave clouds,[35] vigorous convection,[36] and ice fog.[26]

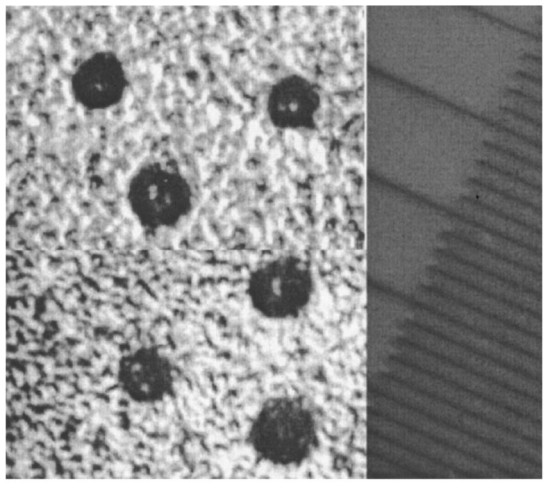

Fig. 1. Replicator images of small ice particles (dark objects in left image) observed for a wave cloud. The distance between the two adjacent lines shown in the right panel is 10 μm. The particle sizes are approximately 30 μm.

To specify the geometry of a general convex particle, we define a coordinate frame that is fixed to the particle (hereafter referred to as the particle frame), as is shown in Fig. 2(a). The origin of this frame coincides with the center of the mass of the ice crystal. The *z* axis of the frame passes through the center of the top face, whereas the corresponding *x* axis points through the midpoint of the line $F'U$. Compared with a pristine hexagonal ice crystal, the geometry of a droxtal is much more complicated because of the presence of 12 isosceles trapezoid faces [e.g., $ABB'A'$ in Fig. 2(a)], six rectangular faces in the center of the crystal, and a top and bottom hexagonal face, for a total of 20 faces. The geometric properties of droxtals having maximum sphericity have been discussed by Yang *et al*.[24] When a particle has maximum sphericity, all the crystal vertices touch a circumscribing sphere. With maximum sphericity, the geometric properties of a droxtal can be fully specified in terms of three parameters, i.e., the radius of the circumscribing sphere R and two angles θ_1 and θ_2 denoted in Fig. 2(b). From the geometric configuration shown in Fig. 2(b) we can obtain the following relationships:

$$a_1 = R \sin \theta_1, \quad a_2 = R \sin \theta_2, \tag{1}$$

$$L_1 = R \cos \theta_1, \quad L_2 = R \cos \theta_2, \tag{2}$$

$$h = a_1(L_1 - L_2)/(a_2 - a_1). \tag{3}$$

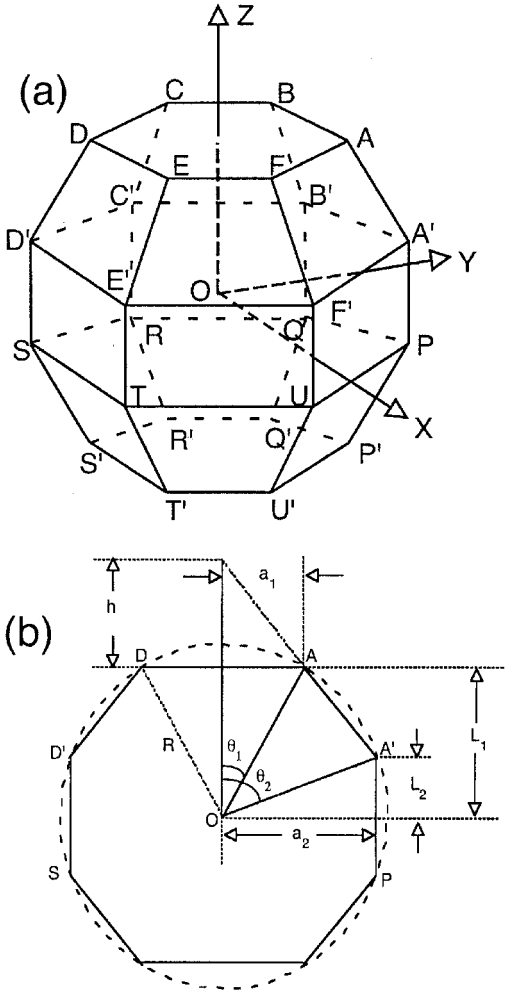

Fig. 2. (a) Geometric representation of a droxtal, (b) cross section of a droxtal (side view).

The quantities in Eqs. (1)–(3) are indicated in Fig. 2(b). The other geometric properties of the droxtal, such as the position vectors of the vertices and the unit vectors normal to the individual faces, can also be specified in terms of R, θ_1, and θ_2. For example, the unit normal vectors $\hat{n}_i = (n_{ix}, n_{iy}, n_{iz})$ associated with the six upper trapezoidal faces of the droxtal can be given as follows:

$$n_{i,x} = \sin\alpha \cos[\pi/2 + (i - 1)\pi/3], \quad (4)$$

$$n_{i,y} = \sin\alpha \sin[\pi/2 + (i - 1)\pi/3], \quad (5)$$

$$n_{i,z} = \cos\alpha, \quad (6)$$

where $i = 1 - 6$ in which $i = 1$ denotes the case for face $ABB'A'$. The parameter α in Eq. (4) is the angle between a unit vector $\hat{n}_{up}$ normal to an upper trapezoidal face (e.g., $ABB'A'$) and the z axis. α can be obtained from a straightforward calculation based on $\alpha = \cos^{-1}(\hat{n}_{up} \cdot \hat{z}) = \cos^{-1}\{2(h + L_1 - L_2)/[3a_2{}^2 + 4(h + L_1 - L_2)^2]^{1/2}\}$. Given the normal vector of each face, the angle between any two different faces of a droxtal can be specified as follows:

$$\phi_{i,j} = \pi - \cos^{-1}(\hat{n}_i \cdot \hat{n}_j), \quad (7)$$

where $\hat{n}_i$ and $\hat{n}_j$ are the normal vectors of surfaces i and j, respectively. In this study, all the normal vectors are defined to be outward pointing from the particle surfaces.

The hexagonal geometry is a special case of the droxtal geometry. For example, as angle θ_1 approaches θ_2, the trapezoidal faces of the droxtal vanish and the particle becomes hexagonal. With appropriate specifications of the three parameters, one can specify hexagonal columns and plates with various aspect ratios and sizes. Similarly, the bottom and top faces can be minimized when θ_1 and θ_2 are properly specified, leading to a double-pyramid shape. Note that some rarely observed halos with angular radii different from 22° and 46° may be attributed to the refraction of rays associated with double-pyramid ice crystals, as articulated by Greenler[37] and references cited therein.

3. Initializing the Ray-Tracing Calculation for Droxtals

The propagating direction of an incident ray with respect to the particle frame (e.g., the coordinate system $oxyz$) can be specified in terms of a unit vector $\hat{r}_i = (\sin\theta_p \cos\beta, \sin\theta_p \sin\beta, \cos\theta_p)$, in which θ_p is the zenith angle measured from the positive z axis to $\hat{r}_i$, and β is the azimuth angle measured from the positive x axis to the projection of $\hat{r}_i$ on the x–y plane. To initialize the ray-tracing calculation for a given localized ray, one must specify the point where the incident ray first hits the particle. The initialization of the ray-tracing calculation in terms of the specification of incident rays and the points where they intersect the crystal surface is straightforward in concept, but is quite complex in its numerical implementation, especially when the particle geometry is complicated. Here we present an efficient method for specifying the incident rays and the initial impinging points on the surface of a general convex particle.

To initialize the ray-tracing calculation associated with a general convex particle, we envision a circular disk that is located at a certain distance from the particle. Let the disk be centered at $-L\hat{r}_i$ where L is a constant and $\hat{r}_i$ is the unit vector pointing along the incident direction. Furthermore, we assume that the radius of this disk is equal to that of the circumscribing sphere of the particle. Any incident ray beginning from a point outside the disk and propagating in the $\hat{r}_i$ direction will pass by the particle without intersecting it. Thus we need to consider only the rays that pass through the region encompassed by the disk. In practice, we randomly select a point within this disk as the starting point for a ray. To cover the disk uniformly with incoming rays, the coordinate values $(x'y'z')$ for the points can

be expressed in the incident coordinate system as follows:

$$x' = R\sqrt{\zeta_3}\cos(2\pi\zeta_4), \tag{8a}$$

$$y' = R\sqrt{\zeta_3}\sin(2\pi\zeta_4), \tag{8b}$$

$$z' = -L, \tag{8c}$$

where R is the radius of the circumscribing sphere of the particle and ζ_3 and ζ_4 are two random numbers uniformly distributed between 0 and 1. To initiate the ray-tracing calculation, the coordinate values have to be transformed to the particle system $oxyz$. The transformation relation is as follows:

$$\begin{bmatrix} x_0 \\ y_0 \\ z_0 \end{bmatrix} = T \begin{bmatrix} x' \\ y' \\ z' \end{bmatrix}, \tag{9}$$

where (x_0, y_0, z_0) is the coordinate values in the particle system and T is the transformation matrix between the two systems that can be specified by

$$T = \begin{bmatrix} \cos\theta_p \cos\beta & -\sin\beta & \sin\theta_p \cos\beta \\ \cos\theta_p \sin\beta & \cos\beta & \sin\theta_p \sin\beta \\ -\sin\theta_p & 0 & \cos\theta_p \end{bmatrix}. \tag{10}$$

If an incident ray starting at (x_0, y_0, z_0) and propagating in the direction of $\hat{r}_i$ can impinge on the droxtal, the ray-tracing calculation is carried out; otherwise, a new incident ray is chosen.

To illustrate the present method for determining whether an arbitrary incident ray can intersect with a convex scattering particle, we consider a simplified two-dimensional scattering problem for which the scattering particle is assumed to be a rectangle. As illustrated in the left panel of Fig. 3(a), an incident ray starting at point O_1 intersects the rectangle. For a given incident direction, the condition for the illumination of a side of the rectangle is that its outward-pointing normal vector must face toward the incoming ray. Thus sides 3 and 4 of the rectangle are prospective sides to be illuminated (hereafter these two sides are referred to as possible sides). Note that sides 1 and 2 can never be illuminated (hereafter these two sides are referred to as impossible sides). Let the distances from point O_1 to the possible sides 3 and 4 be d_3 and d_4 (hereafter possible distances), of which d_3 is larger. Furthermore, let the distances between point O_1 to the impossible sides 1 and 2 be D_1 and D_2 (hereafter impossible distances), of which D_2 is smaller. From the left panel of Fig. 3(a) it is evident that $d_3 < D_2$, i.e., the maximum value for the possible distances is smaller than the minimum value of the impossible distances. However, the opposite situation occurs if the incident ray passes the particle without an intersection, as shown in the right panel of Fig. 3(a). In this case, the maximum value of possible distances is larger than the minimum value of the impossible distances, i.e., $d_3 > D_2$. This geometric property illustrated in the left and right panels of Fig. 3(a) provides a criterion to determine whether an incident ray can intersect with the particle. Mathematically, the criterion can be expressed as follows:

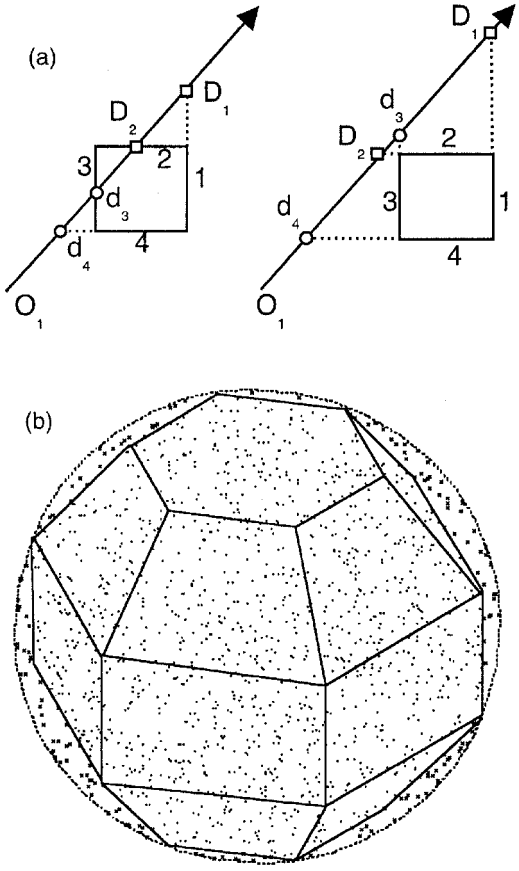

Fig. 3. (a) Conceptual diagram to illustrate the method used to determine whether an incident ray can intersect with a convex scattering particle in the ray-tracing calculation (left panel: the ray intersects with the particle; right panel: the ray passes the particle). (b) The results in which the sampled incident rays impinge on the surface of a droxtal and those that pass the particle without intersecting it.

(1) If $\max(d_i) < \min(D_j)$, an incident ray intersects with the particle, as is the case shown in the left panel of Fig. 3(a).

(2) If $\max(d_i) > \min(D_j)$, an incident ray passes by the particle without intersecting it, as is the case shown in the right panel of Fig. 3(a).

In the preceding criteria, $\max(d_i)$ indicates the maximum value of d_i in which $i = 3$ and 4, whereas $\min(D_j)$ indicates the minimum value of D_j in which $j = 1$ and 2. Note that the values of d_i and D_j can be negative. The present method is suitable for all two- and three-dimensional convex particles no matter how complex the particle surfaces may be. As an example, Fig. 3(b) shows the specification of the incident rays and their corresponding impinging points on a droxtal particle by this method. The circular area bounded by the dotted line indicates the region where starting points of the incident rays are sampled on a plane perpendicular to the direction of in-

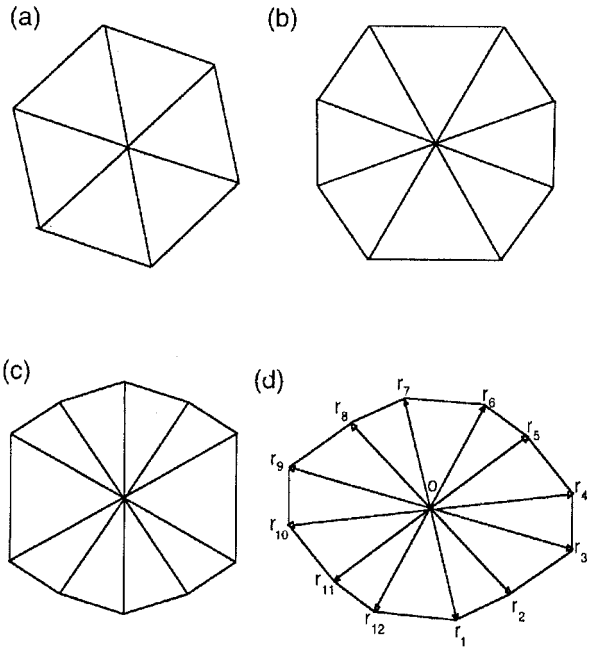

Fig. 4. All possible projections of a droxtal with various orientations relative to the incident direction.

cidence. The solid lines indicate the projection of the droxtal along the incident direction. The dots indicate the projections of the incident rays that intersect with the particle, and the small crosses that are outside the particle projection indicate those incident rays that pass by the particle without intersecting it.

4. Diffraction

The contribution of diffraction to the scattering matrix can be expressed as follows[11]:

$$S_d = \frac{k^2 D}{4\pi}\begin{bmatrix} \cos\theta + \cos^2\theta & 0 \\ 0 & 1 + \cos\theta \end{bmatrix}, \quad (11)$$

$$D = \iint_P \exp(ik\hat{r}_s \cdot \mathbf{r})\mathrm{d}^2 r, \quad (12)$$

where the domain of the integration in Eq. (12), P, is the projected area of the droxtal on a plane perpendicular to the incident direction, k is the wave number, θ is the diffraction angle, $\hat{r}_s$ is a unit vector in the scattering direction, and $\mathbf{r}$ is the position vector of a point in the integration domain. Under different orientation conditions, the projection of a droxtal can vary from a hexagon to a dodecagon, as illustrated in Fig. 4. To perform the integration in Eq. (10) for a specific particle orientation, we divide the projection of the particle onto a plane normal to the incident direction into small triangles that share a vertex at the origin. As an example, let us consider the dodecagonal projection. This projected area can be divided into 12 small triangles. If we denote the 12 apexes of the dodecagon in terms of their position vectors $i = 1 - 13$ [note that $\mathbf{r}_{13} = \mathbf{r}_1$, as shown in Fig. 4(d)], the position vector for an arbitrary point within the ith triangle can be decomposed into two vectors as follows:

$$\mathbf{r} = \varepsilon(1 - \eta)\mathbf{r}_i + \eta\varepsilon\mathbf{r}_{i+1},\ i = 1 - 12, \quad (13)$$

where $\mathbf{r}_i$ and $\mathbf{r}_{i+1}$ constitute the neighboring two sides of the triangle i. Two free parameters $\varepsilon \in \lfloor 0, 1 \rfloor$ and $\eta \in [0, 1]$ are introduced so that any position vector $\mathbf{r}$ in the triangle can be specified by a combination between ε and η. Upon the substitution of Eq. (13) into Eq. (12), the integration of phase variation over these small triangles can be transformed to the integration over the ε and η space. With some mathematical manipulation, it can be shown that

$$\begin{aligned} D_i &= \iint_{\text{triangle}_i} \exp(ik\hat{r}_s \cdot \mathbf{r})\mathrm{d}^2 r = |\mathbf{r}_i \times \mathbf{r}_{i+1}| \\ &\quad \times \int_0^1 \int_0^1 \exp\{ik\hat{r}_s \cdot [\varepsilon(1 - \eta)\mathbf{r}_i + \eta\varepsilon\mathbf{r}_{i+1}]\}\varepsilon\mathrm{d}\eta\mathrm{d}\varepsilon \\ &= \frac{|\mathbf{r}_i \times \mathbf{r}_{i+1}|}{ik\hat{r}_s \cdot (\mathbf{r}_{i+1} - \mathbf{r}_i)}\left[\exp(ik\hat{r}_s \cdot \mathbf{r}_{i+1}/2)\right. \\ &\quad \times \frac{\sin(k\hat{r}_s \cdot \mathbf{r}_{i+1}/2)}{k\hat{r}_s \cdot \mathbf{r}_{i+1}/2} - \exp(ik\hat{r}_s \cdot \mathbf{r}_i/2) \\ &\quad \left. \times \frac{\sin(k\hat{r}_s \cdot \mathbf{r}_i/2)}{k\hat{r}_s \cdot \mathbf{r}_i/2}\right]. \end{aligned} \quad (14)$$

The quantity D in Eq. (12) can be obtained in a straightforward manner when we sum over D_i. One can use the symmetric property of the particle projection to simplify the summation process. We note that $\mathbf{r}_i$ and $\mathbf{r}_{i+6}$ $(i = 1 - 6)$ are oppositely directed about the origin, that is,

$$\mathbf{r}_i = -\mathbf{r}_{i+6},\ i = 1 - 6. \quad (15)$$

This symmetric property of the particle projection will result in the imaginary parts of D_i and D_{i+6} canceling each other in the summation. Thus one can obtain an analytical expression for D as follows:

$$\begin{aligned} D &= \sum_{i=1}^{6} (D_i + D_{i+6}) = \sum_{i=1}^{5} 2|\mathbf{r}_i \times \mathbf{r}_{i+1}| \\ &\quad \times \frac{(\cos q_i - 1)/q_i - (\cos q_{i+1} - 1)/q_{i+1}}{q_{i+1} - q_i} \\ &\quad -2|\mathbf{r}_6 \times \mathbf{r}_1| \frac{(\cos q_6 - 1)/q_6 + (\cos q_1 - 1)/q_1}{q_6 + q_1}, \end{aligned} \quad (16)$$

where $q_i = k\hat{r}_s \cdot \mathbf{r}_i$, in which $i = 1 - 6$. The expression in Eq. (16) is similar to that reported by Yang and Liou[11] for the case of hexagonal ice crystals.

5. Numerical Results and Discussion

The present numerical computation is carried out for two wavelengths at 0.66 and 11 μm, for which the refractive indices of ice[38] are $1.3078 + 1.66 \times 10^{-8} i$

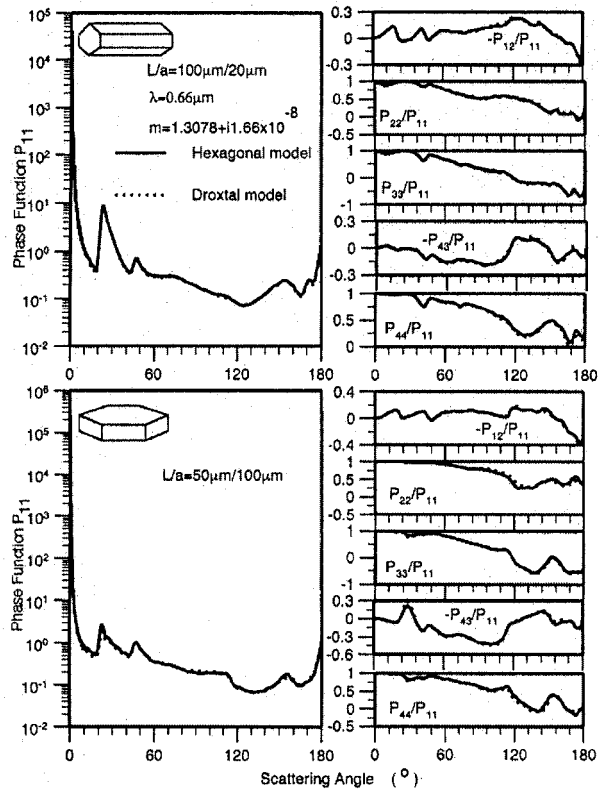

Fig. 5. Phase matrix computed by two models for randomly orientated hexagonal ice columns and plates.

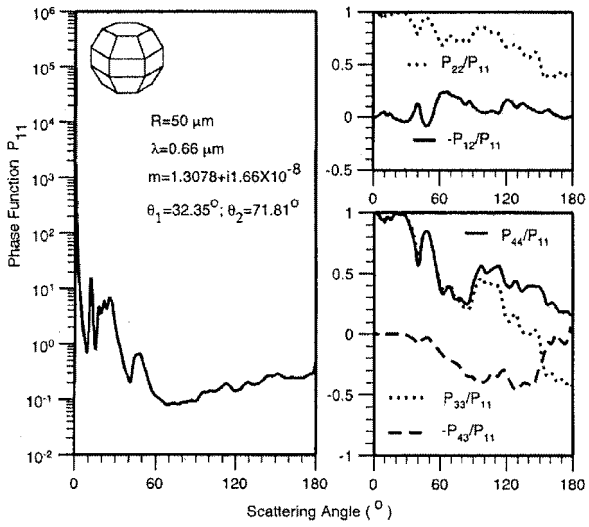

Fig. 6. Nonzero elements of the phase matrix for a droxtal at a wavelength of 0.66 μm with the geometric configuration of $R = 50$ μm, $\theta_1 = 32.35°$, and $\theta_2 = 71.81°$.

and $1.0925 + 2.48 \times 10^{-1}i$, respectively. Because small particles in the atmosphere tend not to have preferred orientations, we assume droxtals to be randomly oriented in space. In the numerical computations we average the single-scattering properties of the particles over 200,000 random orientations.

As discussed in Section 2, hexagonal columns and plates can be viewed as special cases of droxtals with appropriate configurations of θ_1 and θ_2. To validate the IGO method developed in this study, we first compare the results computed from our IGO method with the results by Yang and Liou for hexagons.[34] Figure 5 shows the all-phase matrix elements P_{11}, P_{12}, P_{22}, P_{33}, P_{43}, and P_{44} computed from the two models for randomly orientated hexagonal ice columns ($L/a = 100$ μm/20 μm) and plates ($L/a = 50$ μm/100 μm) at a wavelength of 0.66 μm, where L denotes the length of the column (or the thickness of the plate) and a is the semiwidth of the particle cross section. The droxtal geometry that reduces to the hexagonal column is specified by $R = 53.85$ μm and $\theta_1 = \theta_2 = 21.8°$. For the plate, the corresponding droxtal configuration is $R = 103.12$ μm and $\theta_1 = \theta_2 = 76.0°$. It is evident from Fig. 5 that the phase matrices computed by the two different computational codes are essentially the same.

Figure 6 shows the six nonzero elements of the phase matrix calculated at the wavelength of 0.66 μm for a randomly oriented droxtal ice crystal with $R = 50$ μm and $\theta_1 = 32.35°$ and $\theta_2 = 71.81°$. Note that the size parameter of the droxtal ($2\pi R/\lambda$) is approximately 476 in this case. For a given value of R, a droxtal with these values of θ_1 and θ_2 possesses the maximum possible volume. For the phase function P_{11}, the strong forward scattering is caused by diffraction and also by the refraction through various pairs of parallel crystal faces. A pronounced scattering peak can be seen at a scattering angle of 11°. This peak is also observed for the phase function of an individual bullet-shaped crystal and also bullet rosettes.[8,39] The minimum deviation angle θ_m associated with ray refraction through two faces inclined at an angle Δ can be calculated by the following equation:[40]

$$\theta_m = 2 \sin^{-1}\left(m \sin\frac{\Delta}{2}\right) - \Delta, \qquad (17)$$

where m is the real part of the refractive index. Based on Eq. (17), the peak at 11° can be explained by two sequential refractions through a trapezoidal face such as $ABB'A'$ and a rectangular face such as $D'E'TS$ [see Fig. 2(a)]. These two faces are inclined at an angle of 34°, and the corresponding minimum-deviation angle for a real refractive index $m = 1.3078$ is 11°. Three small peaks are seen over a broad scattering maximum that ranges from 16° to 26° including the 22° halo. The other two scattering maxima at 16° and 26° can be explained by the minimum-deviation angles associated with two sequential refractions of rays through a prism angle of 48° and 68°, respectively. The angles between any two faces of a droxtal with $\theta_1 = 32.35°$ and $\theta_2 = 71.81°$ are listed in Table 1, which also lists the minimum-deviation angles calculated by Eq. (17) with the refractive index of ice at 0.66 μm. The broad scattering maxima region in the phase function between 16° and 26° is the result of contributions by five possible face combinations. There are three possible combinations that contribute to the scattering maxima around 46°. Because of the presence of 12 trapezoidal faces and

Table 1. Minimum-Deviation Angles Associated with Various Combinations of the Particle Faces

Angle Δ	Face Combination	Minimum-Deviation Angle θ_m
0°	Top–bottom	0°
	ABB′ A′–STT′ S′	
	A′ B′ QP–D′ E′ TS	
34°	*ABB′ A′–D′ E′ TS*	11°
48°	*ABB′ A′–RSS′ R′*	16°
56°	*ABB′ A′*–bottom	19.8°
	PQQ′ P′–top	
60°	*A′ B′ QP–C′ D′ SR*	21.7°
65.5°	*ABB′ A′–C′ D′ SR*	24.6°
68°	*ABB′ A′–DEE′ D′*	26°
88°	*ABB′ A′–CDD′ C′*	42.6°
90°	*A′ B′ QP*–top	46°
	A′ B′ QP–bottom	
91.8°	*ABB′ A′–QRR′ Q′*	48°
112°	*ABB′ A′–PQQ′ P′*	
114.5°	*ABB′ A′–B′ C′ RQ*	
120°	*A′ B′ QP–B′ C′ RQ*	
124°	*ABB′ A′*–top	
	PQQ′ P′–bottom	
131°	*ABB′ A′–BCC′ B′*	

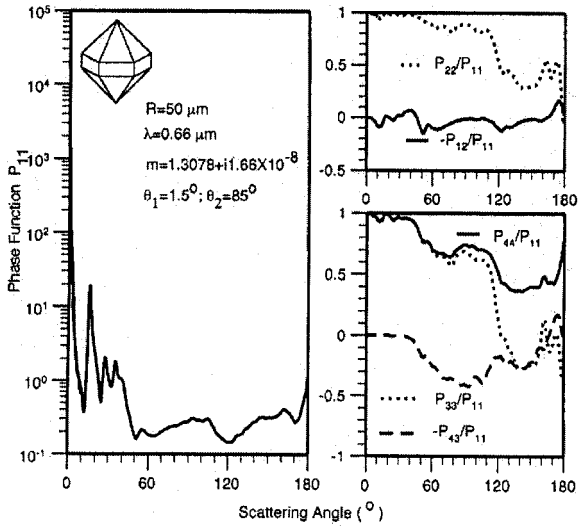

Fig. 7. Nonzero elements of the phase matrix for a droxtal at a wavelength of 0.66 μm with the geometric configuration of $R = 50$ μm, $\theta_1 = 1.5°$, and $\theta_2 = 85°$.

the decrease of the portion of rectangular crystal surfaces for droxtals in comparison with hexagons, the scattering maximum at 150° caused by multiple total internal reflections becomes much smaller than that in the case for hexagons. The degree of linear polarization can be represented by $-P_{12}/P_{11}$ when the incident ray is unpolarized. Figure 6 shows that a negative polarization is associated with the 22° and 46° halos and in the vicinity of pure backscatter (180°). The element P_{22}/P_{11} is related to the depolarization of scattering light when the incident rays are linearly polarized. This element is also a good indicator of the nonsphericity of the droxtal. Positive values are noted for P_{22}/P_{11} for the entire scattering angular domain. Values for element $-P_{43}/P_{11}$ are essentially negative, except for a small positive peak located in the vicinity of 177°. The values of P_{33}/P_{11} and P_{44}/P_{11} are approximately equal for the scattering angles ranging from 0° to 90°. At scattering angles larger than 90°, P_{33}/P_{11} becomes negative, whereas P_{44}/P_{11} remains positive. Because of the hexagonal structure, the phase-matrix elements of droxtals are similar to those of hexagons, as is evident from a comparison of the present results and those shown by Takano and Jayaweera.[5]

Figure 7 shows the scattering phase matrix of a droxtal with $R = 50$ μm, $\theta_1 = 1.5°$, and $\theta_2 = 85°$ at the 0.66-μm wavelength. Because θ_1 is very small, the top and bottom faces essentially shrink to a point, and the surface area of each of the pyramidal faces is substantially increased. Thus there are 18 faces for this configuration compared with the 20 faces discussed above. Compared with the phase function of the droxtal shown in Fig. 6, the forward-scattering maximum for this crystal is slightly larger because of an increase in the diffracted energy. A pronounced scattering peak located at 15° can be seen for P_{11}, whose formation mechanism is similar to that for the 11° halo in Fig. 6. Because of the absence of the top and bottom faces, the scattering maximum near 46° caused by the refraction through the top or bottom faces and a central face is negligible. The increase in the area of the trapezoidal faces reduces the scattering peak corresponding to the 22° halo. By comparing the phase functions shown in Figs. 6 and 7, one can see significant differences for scattering angles ranging from 140° to 160°. For other phase-matrix elements, the overall features shown in Figs. 6 and 7 are similar. However, significant differences can be seen in the backscattering direction for these two cases, particularly for P_{44}/P_{11} and P_{22}/P_{11}. This behavior may have implications for measurements by depolarized lidars.

The asymmetry factors for the droxtals shown in Figs. 6 and 7 are 0.8038 and 0.7459, respectively, and are smaller than that of the spherical ice crystals (0.8911) having the same size. In the GO region, the asymmetry factor is more sensitive to the geometric shape than the size of the particle. These differences in the asymmetry factor may have an influence on the determination of the radiative forcing of cirrus clouds. If the smallest ice crystals in a given size distribution are assumed to be spherical, one may introduce substantial errors in the climate model or in the interpretation of the remote sensing measurements involving cirrus clouds.

Figures 8 and 9 show the nonzero elements of the phase matrix for two different droxtal geometries at the infrared (IR) wavelength of 11 μm. Compared with those calculated at a visible wavelength, phase functions in the IR are essentially featureless in the side-scattering and backscattering directions. This behavior can be ascribed to substantial absorption within the ice particles at this wavelength, which acts

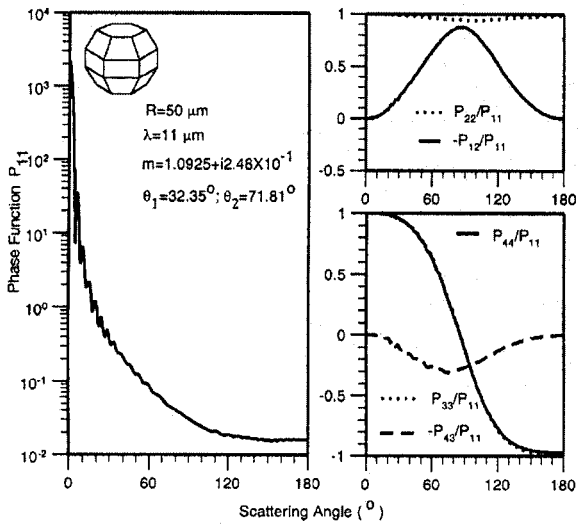

Fig. 8. Nonzero elements of the phase matrix for a droxtal at a wavelength 11 μm with the geometric configuration of $R = 50$ μm, $\theta_1 = 32.35°$, and $\theta_2 = 71.81°$.

to attenuate the energy of the rays refracted into the particle to a negligible amount. Because diffracted energy is concentrated in the forward direction, the phase matrices in the side-scattering and backscattering directions are essentially attributed to the external reflection of rays.[41] The oscillation in the phase function P_{11} is associated with the diffraction component of the scattered energy. The present results confirm that, in the IR, detailed geometric information of the particle such as edges and corners becomes less important and the diffraction component of scattering dominates the pattern of the phase function, as has been noted in previous studies (e.g., Lee *et al.*[42]). As evident from Figs. 8 and 9, the phase-matrix elements associated with the polarization configuration of scattered light are insensitive to the detailed particle geometry. The feature associated with external reflection is insensitive to the particle geometry under the assumption of random particle orientation.

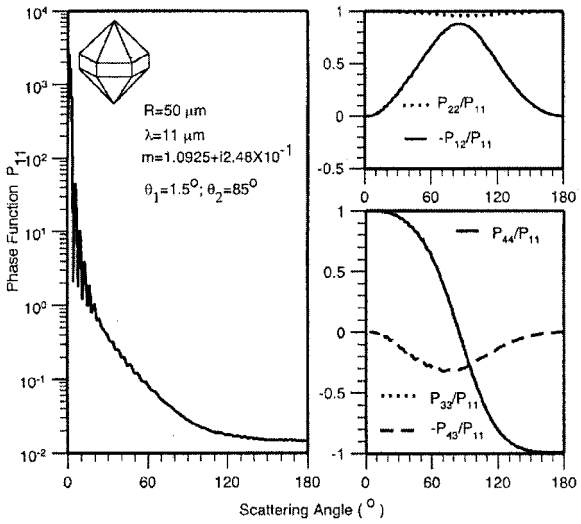

Fig. 9. Nonzero elements of the phase matrix for droxtals at 11 μm with the geometric configuration of $R = 50$ μm, $\theta_1 = 1.5°$, and $\theta_2 = 85°$.

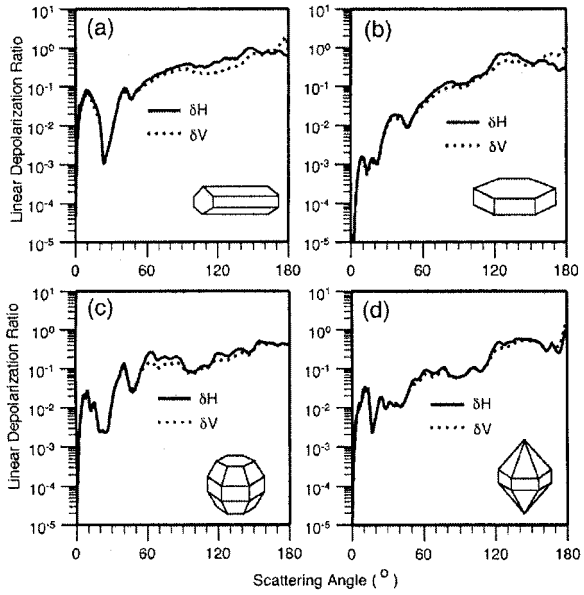

Fig. 10. Linear depolarization ratio for droxtal and hexagonal ice crystals.

Figure 10 shows the linear depolarization ratios δH and δV for four types of ice crystal (hexagonal columns, plates, 20-faced droxtal, and 18-faced droxtal), where δH and δV are defined, respectively, as follows[5]:

$$\delta H = \frac{P_{11} - P_{22}}{P_{11} + 2P_{12} + P_{22}}, \tag{18a}$$

$$\delta V = \frac{P_{11} - P_{22}}{P_{11} - 2P_{12} + P_{22}}. \tag{18b}$$

For hexagonal columns and plates, there is a notable difference between δV and δH at a nearly backward-scattering angle (i.e., $\theta \approx 178°$), whereas for the droxtals the difference is not as pronounced. Because of the hexagonal structures, the values of δV and δH for all crystals display peaks in the angular region $2° < \theta < 20°$. This phenomenon has been discussed by Takano and Jayaweera.[5] At the backscattering angle $\theta = 180°$, linear depolarization ratios for droxtals with $\theta_1 = 32.35°$ and $\theta_2 = 71.81°$ (i.e., the 20-faced droxtal) have the smallest value among these four kinds of ice crystal, and the 18-faced droxtal with $\theta_1 = 1.5°$ and $\theta_2 = 85°$ has the largest values. These differences in the backscattering direction may have implications for the interpretation of polarized lidar returns when ice clouds are present. Interestingly, 20- and 18-faced droxtals exhibit different patterns of linear depolarization ratios in the near-backscattering direction. Although δH and δV of the former show virtually no angular dependence for scattering angles larger than 160°, linear depolarization ratios of the latter increase drastically for scattering angles approaching 180°. As was shown previously,[43] such gradients in the azi-

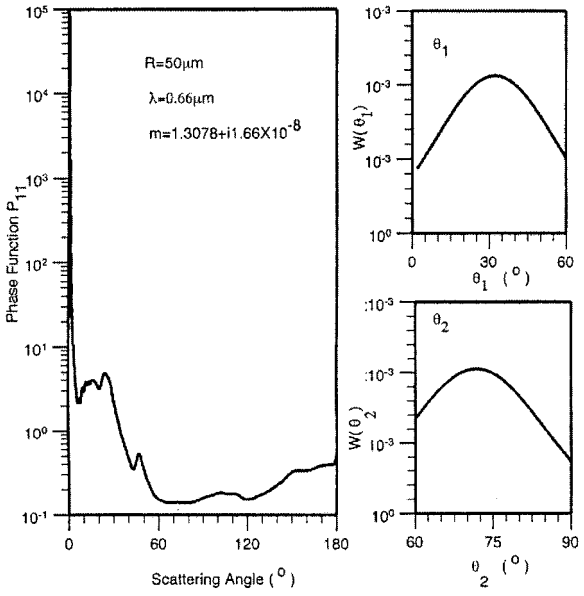

Fig. 11. Phase function of droxtals derived from the averaging of various combinations of θ_1 and θ_2.

muthally integrated linear depolarization ratio affect cirrus polarization measurements with lidar because photons contribute to the signals that are scattered more than once in the cloudy atmosphere. However, for optically thin (translucent) cirrus clouds, this multiple-scattering error is small.

In reality, the geometry of droxtal ice crystals cannot be confined to a specific combination of θ_1 and θ_2. Figure 11 shows the average of the 0.66-μm phase function P_{11} over various combinations of θ_1 and θ_2. As shown in Fig. 11, the values of θ_1 and θ_2 are assumed to follow two Gaussian distributions centered at 32.35° and 71.81°, respectively. These distributions for θ_1 and θ_2 imply that droxtals with the maximum-volume configuration (i.e., $\theta_1 = 32.35°$ and $\theta_2 = 71.81°$) are the most prevalent among all possible droxtal configurations in cirrus clouds. Let $W_1(\theta_1)$ and $W_2(\theta_2)$ be the probability weightings specified by the Gaussian distributions. The average phase function can be obtained as follows:

$$\bar{P}_{11}(\theta_s) = \frac{\int_{\theta_1}\int_{\theta_2} P_{11}(\theta_s;\, \theta_1,\, \theta_2) W_1(\theta_1) W_2(\theta_2) \sigma_s(\theta_1,\, \theta_2) \mathrm{d}\theta_1 \mathrm{d}\theta_2}{\int_{\theta_1}\int_{\theta_2} W_1(\theta_1) W_2(\theta_2) \sigma_s(\theta_1,\, \theta_2) \mathrm{d}\theta_1 \mathrm{d}\theta_2}, \tag{19}$$

where σ_s is the single-scattering cross section. The 22° and 46° halos become pronounced in the averaged phase function $\bar{P}_{11}$. We also note that the average over different geometric configurations smoothes out the scattering peaks occurring at small angles such as 11°, as well as those small oscillations in side-scattering and backscattering directions. Compared with the case for hexagonal ice crystals, the scattering phase function averaged over various droxtal configurations is quite unique, particularly in the 22°, 150°, and backscattering angular regions.

6. Conclusions

Small particles with aspect ratios of the order of unity are prevalent in the uppermost regions of mid-latitude and tropical cirrus clouds. The scattering behavior of these small ice crystals is important to the understanding of the bulk optical properties of cirrus clouds and the remote sensing of these cloud microphysical and optical properties from satellite or surface measurements. Multifaced ice crystals known as droxtals are suggested to represent these small ice crystals. The single-scattering properties of droxtals were investigated previously through an application of the FDTD method, but the results were limited to small size parameters less than 20. In this study we employ an IGO model[34] to investigate the single-scattering properties of droxtals with size parameters in the GO region. Two different shapes are considered in which the particles have either 18 or 20 faces. An efficient approach is presented for the initialization of the ray-tracing calculations for a particle having a general convex shape.

The phase function of the droxtals at the visible wavelength (0.66 μm) displays maxima at scattering angles smaller than 22°. The maxima can be explained by consideration of two sequential refractions associated with the pyramidal and columnar faces. Because of the hexagonal structure of the crystal facets, all elements of the scattering phase matrix show similarities to the properties that have been observed in those of hexagonal ice crystals. At 11 μm, where absorption of the incident radiation within the particle becomes dominant, the phase functions of the 18- and 20-faced droxtals are essentially featureless. A comparison of the linear depolarization at a visible wavelength between hexagonal and droxtal ice crystals suggests that there is a notable difference at the backscattering angles. This difference is also observed between droxtals with different geometric configurations (i.e., the 18- and 20-faced crystals). Finally, we note that the average of the phase function over various geometric configurations effectively smoothes out the small oscillations, especially in the backscattering angles.

This study is supported by a National Science Foundation (NSF) CAREER Award research grant (ATM-0239605) from the NSF Physical Meteorology Program managed by William A. Cooper and by research grants (NAG-1-02002 and NAG5-11374) from the NASA Radiation Sciences Program managed by Donald Anderson. G. W. Kattawar's research is supported by the U.S. Office of Naval Research under contract N00014-02-1-0478.

References

1. K. N. Liou, "Influence of cirrus clouds on weather and climate processes: a global perspective," Mon. Weather Rev. **114,** 1167–1199 (1986).

2. D. K. Lynch, K. Sassen, D. O. Starr, and G. Stephens, eds., *Cirrus* (Oxford U. Press, New York, 2002).
3. P. Wendling, R. Wendling, and H. K. Weikman, "Scattering of solar radiation by hexagonal ice crystals," Appl. Opt. **18,** 2663–2671 (1979).
4. Q. Cai and K. N. Liou, "Theory of polarized light scattering by hexagonal ice crystals," Appl. Opt. **21,** 3569–3580 (1982).
5. Y. Takano and K. Jayaweera, "Scattering phase matrix for hexagonal ice crystals computed from ray tracing," Appl. Opt. **24,** 3254–3263 (1985).
6. Y. Takano and K. N. Liou, "Solar radiative transfer in cirrus clouds. Part I. Single-scattering and optical properties of hexagonal ice crystals," J. Atmos. Sci. **46,** 3–19 (1989).
7. A. Macke, "Scattering of light by polyhedral ice crystals," Appl. Opt. **32,** 2780–2788 (1993).
8. A. Macke, J. Mueller, and E. Raschke, "Single scattering properties of atmospheric ice crystals," J. Atmos. Sci. **53,** 2813–2825 (1996).
9. K. Muinonen, "Scattering of light by crystals: a modified Kirchhoff approximation," Appl. Opt. **28,** 3044–3050 (1989).
10. M. Hess, R. B. A. Koelemeijer, and P. Stammes, "Scattering matrices of imperfect hexagonal crystals," J. Quant. Spectrosc. Radiat. Transfer **60,** 301–308 (1998).
11. P. Yang and K. N. Liou, "Single-scattering properties of complex ice crystals in terrestrial atmosphere," Contrib. Atmos. Phys. **71,** 223–248 (1998).
12. M. I. Mishchenko, W. B. Rossow, A. Macke, and A. A. Lacis, "Sensitivity of cirrus cloud albedo, bidirectional reflectance, and optical thickness retrieval to ice-particle shape," J. Geophys. Res. **101,** 16973–16985 (1996).
13. K. N. Liou, Y. Takano, and P. Yang, "2000: light scattering and radiative transfer by ice crystal clouds: applications to climate research," in *Light Scattering by Nonspherical Particles: Theory, Measurements, and Geophysical Applications*, M. I. Mishchenko, J. W. Hovenier, and L. D. Travis, eds. (Academic, San Diego, Calif., 2000), Chap. 15, pp. 417–449.
14. A. J. Heymsfield and J. Iaquinta, "Cirrus crystal terminal velocities," J. Atmos. Sci. **57,** 916–938 (2000).
15. P. R. Lawson, B. A. Baker, C. G. Schmitt, and T. J. Jensen, "An overview of microphysical properties of Arctic clouds observed in May and July 1998 during FIRE ACE," J. Geophys. Res. **106,** 14989–15014 (2001).
16. E. J. Jensen, O. B. Toon, H. B. Selkirk, J. D. Spinhirne, and M. R. Schoeberl, "On the formation and persistence of subvisible cirrus clouds near the tropical tropopause," J. Geophys. Res. **101,** 21361–21375 (1996).
17. A. J. Heymsfield, "Cirrus uncinus generating cells and the evolution of cirriform clouds. Part I: Aircraft observations of the growth of the ice phase," J. Atmos. Sci. **32,** 799–808 (1975).
18. A. J. Heymsfield, K. M. Miller, and J. D. Spinhirne, "The 27–28 October 1986 FIRE IFO cirrus case study: cloud microstructure," Mon. Weather Rev. **118,** 2313–2328 (1990).
19. P. Yang, B.-C. Gao, B. A. Baum, W. Wiscombe, Y. Hu, S. L. Nasiri, A. Heymsfield, G. McFarquhar, and L. Miloshevich, "Sensitivity of cirrus bidirectional reflectance in MODIS bands to vertical inhomogeneity of ice crystal habits and size distributions," J. Geophys. Res. **106,** 17267–17291 (2001).
20. G. M. McFarquhar, P. Yang, A. Macke, and A. J. Baran, "A new parameterization of single-scattering solar radiative properties for tropical anvils using observed ice crystal size and shape distributions," J. Atmos. Sci. **59,** 2458–2478 (2002).
21. M. I. Mishchenko, "Light scattering by size–shape distributions of randomly oriented axially symmetric particles of a size comparable to wavelength," Appl. Opt. **32,** 623–625 (1993).
22. J. Reichardt, S. Reichardt, P. Yang, and T. J. McGee, "Retrieval of polar stratospheric cloud microphysical properties from lidar measurements: dependence on particle shape assumptions," J. Geophys. Res. **107D,** 10.1029/2001JD001021 (2002).
23. L. Liu and M. I. Mishchenko, "Constraints on PSC particle microphysics derived from lidar observations," J. Quant. Spectrosc. Radiat. Transfer **70,** 817–831 (2001).
24. P. Yang, B. A. Baum, A. J. Heymsfield, Y.-X. Hu, H.-L. Huang, S.-C. Tsay, and S. A. Ackerman, "Single scattering properties of droxtals," J. Quant. Spectrosc. Radiat. Transfer **79–80,** 1159–1169 (2003).
25. W. C. Thuman and E. Robinson, "Studies of Alaskan ice-fog particles," J. Meteorol. **11,** 151–156 (1954).
26. T. Ohtake, "Unusual crystal in ice fog," J. Atmos. Sci. **27,** 509–511 (1970).
27. W. Sun and Q. Fu, "Finite-difference time-domain solution of light scattering by dielectric particles with large complex refractive indices," Appl. Opt. **39,** 5569–5578 (2000).
28. M. I. Mishchenko, J. W. Hovenier, and L. D. Travis, *Light Scattering by Nonspherical Particles* (Academic, San Diego, Calif., 2000).
29. F. M. Kahnert, "Numerical methods in electromagnetic scattering theory," J. Quant. Spectrosc. Radiat. Transfer **79–80,** 775–824 (2003).
30. M. I. Mishchenko and A. Macke, "How big should hexagonal ice crystals be to produce halos?" Appl. Opt. **38,** 1626–1629 (1999).
31. S. Havemann, A. J. Baran, and J. M. Edwards, "Implementation of the T-matrix method on a massively parallel machine: a comparison of hexagonal ice cylinder single-scattering properties using the T-matrix and improved geometric optics methods," J. Quant. Spectrosc. Radiat. Transfer **79–80,** 707–720 (2003).
32. P. Yang and K. N. Liou, "Light scattering by hexagonal ice crystals: comparison of finite-difference time domain and geometric optics methods," J. Opt. Soc. Am. A **12,** 162–176 (1995).
33. P. Yang and K. N. Liou, "Finite-difference time domain method for light scattering by small ice crystals in three-dimensional space," J. Opt. Soc. Am. A **13,** 2072–2085 (1996).
34. P. Yang and K. N. Liou, "Geometric-optics integral-equation method for light scattering by nonspherical ice crystals," Appl. Opt. **35,** 6568–6584 (1996).
35. A. J. Heymsfield and L. M. Miloshevich, "Homogeneous ice nucleation and supercooled liquid water in orographic wave clouds," J. Atmos. Sci. **50,** 2335–2353 (1993).
36. D. Rosenfeld and W. L. Woodley, "Deep convective clouds with sustained supercooled liquid water down to −37.5 degrees," Nature (London) **405,** 440–442 (2000).
37. R. Greenler, *Rainbows, Halos and Glories* (Cambridge U. Press, Cambridge, UK, 1980).
38. S. G. Warren, "Optical constants of ice from the ultraviolet to the microwave," Appl. Opt. **23,** 1206–1225 (1984).
39. J. Iaquinta, H. Isaka, and P. Personne, "Scattering phase function of bullet rosette ice crystals," J. Atmos. Sci. **52,** 1401–1413 (1995).
40. K. N. Liou, *Introduction to Atmospheric Radiation* (Academic, New York, 1980).
41. P. Yang, B.-C. Gao, B. A. Baum, Y. X. Hu, W. J. Wiscombe, M. I. Mishchenko, D. M. Winker, and S. L. Nasiri, "Asymptotic solutions for optical properties of large particles with strong absorption," Appl. Opt. **40,** 1532–1547 (2001).
42. Y. K. Lee, P. Yang, M. I. Mishchenko, B. A. Baum, Y. Hu, H.-L. Huang, W. J. Wiscombe, and A. J. Baran, "Use of circular cylinders as surrogates for hexagonal pristine ice crystals in scattering calculations at infrared wavelengths," Appl. Opt. **42,** 2653–2664 (2003).
43. S. Reichardt and J. Reichardt, "Effect of multiple scattering on depolarization measurements with spaceborne lidars," Appl. Opt. **42,** 3620–3633 (2003).